Energy & Environmental Science

ROYAL SOCIETY OF CHEMISTRY

COMMUNICATION

View Article Online
View Journal

Cite this: DOI: 10.1039/d2ee02557d

Received 9th August 2022,
Accepted 19th October 2022

DOI: 10.1039/d2ee02557d

rsc.li/ees

Energy autonomous paper modules and functional circuits†

Jing Han,‡[ab] Nuo Xu,‡[ac] Jinran Yu,[ab] Yifei Wang,[ab] Yao Xiong,[ab] Yichen Wei,[ac] Zhong Lin Wang *[abd] and Qijun Sun *[abc]

Energy-efficient intelligent systems incorporating modern electronics, circuits, and power sources have rapidly become inseparable for a wide range of applications. Here, we propose a prototype of energy autonomous functional paper modules, which comprise triboelectric energy harvester, power management circuits (PMCs), energy storage units, and back-end functional circuits. Each of the paper modules has its specific function and can be used individually, incorporated, or replaced/selected depending on different circumstances. The fabricated paper modules are ready to convert mechanical energy into electricity through the paper-based triboelectric nanogenerator (paper-TENG) unit; the converted AC output can be delivered to the PMC paper module and regulated into DC output to improve the charging efficiency for energy storage units; the stored electrochemical energy can be successfully used to drive the back-end module of functional circuits (including flowing LEDs, temperature/humidity sensors, and wireless transmitters). The working process of the sustainable paper modules implies an energy circulation of mechanical energy conversion, electrochemical energy storage, and energy utilization in functional circuits (in the form of photonic, thermal, electromagnetic, or mechanical energy). The proposed energy-autonomous functional paper modules present new paradigm for sustainable and adaptive functional circuits to extend the broader path toward efficient, economical, and customized integrative electronics and complementary self-powered systems.

Broader context

Energy-efficient intelligent systems incorporating modern electronics, circuits, and power sources have rapidly become inseparable for a wide range of applications. Here, we propose a prototype of energy autonomous functional paper modules, which comprise triboelectric energy harvester, power management circuits (PMCs), energy storage units, and back-end functional circuits. Each of the paper modules has its specific function and can be used individually, incorporated, or replaced/selected depending on different circumstances. The fabricated paper modules are ready to convert mechanical energy into electricity through the paper-based triboelectric nanogenerator (paper-TENG) unit; the converted AC output can be delivered to the PMC paper module and regulated into DC output to improve the charging efficiency for energy storage units; the stored electrochemical energy can be successfully used to drive the back-end module of functional circuits (including flowing LEDs, temperature/humidity sensors, and wireless transmitters). The working process of the sustainable paper modules implies an energy circulation of mechanical energy conversion, electrochemical energy storage, and energy utilization in functional circuits (in the form of photonic, thermal, electromagnetic, or mechanical energy). The proposed energy-autonomous functional paper modules present new paradigm for sustainable and adaptive functional circuits to extend the broader path toward efficient, economical, and customized integrative electronics and complementary self-powered systems.

1. Introduction

Modern electronics have moved into a multiplex-developing era in which device scaling (or cost reduction) is not the only path followed by the semiconductor industry in the last few decades.[1] In particular, transistor scaling approaching the 3 nm limitation urgently requires revolutionary technology to transcend Moore's law by improving cost/performance efficiency with novel nanomaterials or adding more functionality through integration.[2,3] Emerging "More than Moore" toward diversity and versatility is leading another research direction to advance information technology through the rapid development of wearable smart devices and systems,[4,5] artificial intelligence,[6] biomimetic electronics,[7,8] neuromorphic transistors,[9] adaptive

[a] Beijing Institute of Nanoenergy and Nanosystems, Chinese Academy of Sciences, Beijing, 101400, China. E-mail: sunqijun@binn.cas.cn, zhong.wang@mse.gatech.edu
[b] School of Nanoscience and Technology, University of Chinese Academy of Sciences, Beijing, 100049, China
[c] Center on Nanoenergy Research, School of Physical Science and Technology, Guangxi University, Nanning, 530004, China
[d] School of Materials Science and Engineering, Georgia Institute of Technology, Atlanta, Georgia 30332-0245, USA

† Electronic supplementary information (ESI) available. See DOI: https://doi.org/10.1039/d2ee02557d

‡ These authors contributed equally to this work.

interactive interfaces,[10] and self-powered E-textiles.[11] The More-than-Moore devices and intelligent systems, which incorporate power sources, power electronics, multifunctional sensors, and wireless transmitters, have become increasingly prominent with functional diversification in systematic integration and cost/performance advantages.[12–16] Intelligent functional systems have rapidly gained great significance in a variety of applications, *e.g.*, health supervision,[17] wellness-monitoring,[18] disease prevention,[19] robotic exoskeletons,[20] smart prosthetics,[21] and interactive equipment for virtual reality.[22] Meanwhile, the energy efficiency of these integrated systems has also emerged as a significant task/target to go beyond the inconvenience and possible pollution problems of traditional power supply.[23–25] The associated development in energy harvesting techniques, progressive energy storage devices, and low-power-consuming functional electronics offers an efficient means to constitute the anticipated energy-autonomous system.[26–28] Commonly, the sustainable operation of integrated functional systems is guaranteed by the specific components as follows: (i) energy harvesters relying on photovoltaics,[29] piezoelectric transducers,[30] triboelectric nanogenerators,[31] or thermoelectric devices;[32] (ii) energy storage devices with batteries[33] or supercapacitors;[34] (iii) power management strategy and low-power-consuming electronics;[23] and (iv) economy and recyclable substrate materials.[35]

Paper electronics have attracted considerable attention due to the unique characteristics of conjugated paper substrates, including mechanical flexibility/foldability, sustainability, biodegradability, light weight, low cost, *etc.*[35–37] It offers an excellent on-chip prototype with facile modular design and potential energy-autonomy characteristics, covering paper-based printed circuit boards,[38] hybridized electronics/microfluidics,[39] nano/microelectromechanical systems,[40] and various energy harvesters. Paper-based triboelectric nanogenerators (TENGs),[31] booming prosperously in recent years, are ready to harvest low-frequency and high-entropy mechanical energy from biomechanical motions and the surrounding environment, *e.g.*, palming, walking, blow-wind, raindrops, *etc.*[41–43] Taking advantage of contact-electrification-activation, TENGs have led the innovative technical roadmap to micro/nano power sources,[44] self-powered systems,[45] high-voltage sources,[46] blue energy,[47] and recently emerging interface spectroscopy.[48] However, there are still some challenges to the optimization of energy conversion/utilization in paper-based energy-autonomous systems due to the intrinsic AC outputs from triboelectric energy harvesters. Therefore, it is necessary to minimize the loss of harvested/received energy and optimize the energy consumption of global/local electronic components from the level of system integration. Pairing a proper power management strategy with energy harvesters offers an effective means to break through the bottleneck of mismatching between TENG output characteristics (low current) and the power requirement for terminal electronics (high current).[49] Accordingly, modular integration of power management, energy storage, and functional components can maximize the energy transfer/conversion efficiency and bridge energy harvesting, storage, and utilization on the integrated paper modules at the system level.[23]

Here, we propose a sustainable and energy-autonomous paper-based functional circuits in modular layout, which consists of a TENG energy harvester, power management circuits (PMCs), energy storage units, and functional circuit (FC) modules. All the functional units are constructed on Teslin paper substrates, with the basic electronic components connected *via* scalable/designable electrodes prepared by facile and high-throughput laser engraving technique. The fabricated paper modules are ready to harvest low-frequency and high-entropy (bio)mechanical energy through an accessible but efficient paper-TENG unit; the converted alternating output (in intrinsic low-current and high-voltage characteristics) can be delivered to the designed power management circuit on paper (*i.e.*, PMC paper module); the PMC module regulates the AC output into a steady and continuous DC output through the PMC module for improving charging efficiency (or energy utilization efficiency) in electrochemical energy storage units; the stored electrochemical energy can be successfully used to drive the back-end functional circuits (including flowing LEDs, temperature/humidity sensors, and wireless transmitters). The working process of the paper modules embodies a sustainable energy circulation fashion of energy harvesting, management, storage, and utilization in different energy-forms. The proposed energy-autonomous functional paper modules present a new paradigm for paper-based sustainable and adaptive functional circuits, which will extend the broader path toward efficient, economical, and customized integrative multifunctional electronics and complementary self-powered systems.

2. Results and discussion

2.1 Modular layout of the sustainable paper-based functional circuits

The demonstrated sustainable functional paper modules are schematically illustrated in Fig. 1(a), including four regular components in modular design, *i.e.*, the paper-TENG energy harvester, the designed power management circuits on-paper, planar electrochemical energy storage devices, and the integrated functional terminals (marked with Modules 1–4, respectively). The functional paper modules are capable of harvesting surrounding (bio)mechanical energy, converting it into DC output for efficient energy storage in micro-supercapacitors (MSCs) or batteries, and driving the back-end functional circuits (including flowing LEDs, temperature/humidity sensors, and wireless transmitters). Combining the demanded functional circuits, the incorporated paper modules can readily work in an energy-autonomous way, *i.e.*, sustainable functional paper modules. The functional paper modules can be implemented either in a discrete-unit fashion or as a customized integration style. Its working process implies an energy circulation from mechanical energy conversion into AC electricity (regulated into DC output), energy storage in electrochemical form, and energy utilization in functional circuits (in the form of photonic, thermal, electromagnetic, or mechanical energy, Fig. 1(b)). The energy-autonomous and adaptive paper modules provide new electronic prototypes and paradigm to augment conventional printed circuit broads

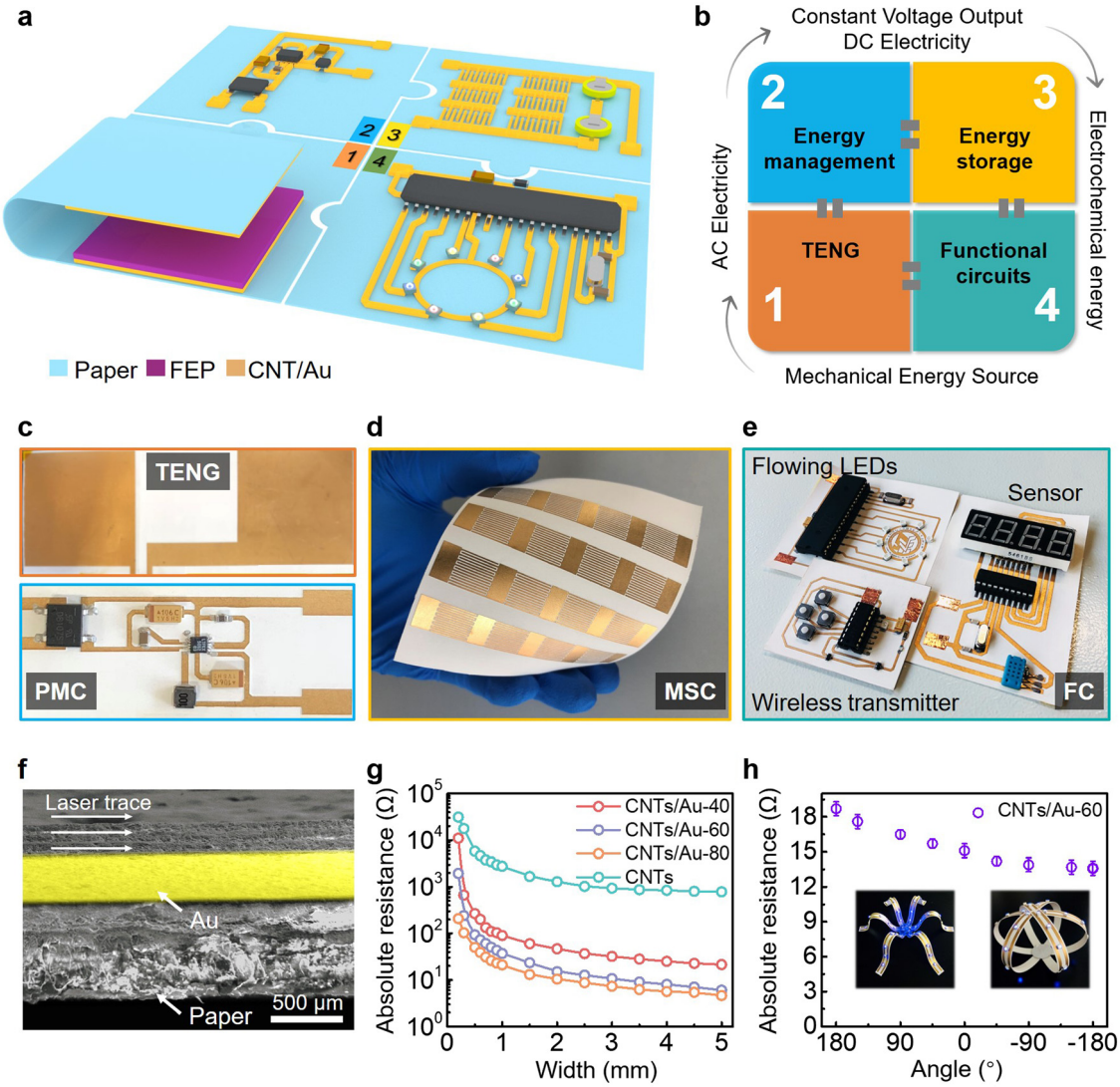

Fig. 1 Schematic illustration of the sustainable functional paper modules. (a) Schematic illustration of the sustainable functional paper modules. (b) Energy circulation diagram for the sustainable paper modules. Photo images of the fabricated regular paper modules: (c) paper-based triboelectric nanogenerator (paper-TENG) and power management circuit (PMC); (d) microsupercapacitors (MSCs); (e) functional circuits (FC) modules for flowing LEDs, temperature/humidity sensor, and IR emitters. (f) Cross-sectional SEM image of the interface between CNT/Au hybrid electrodes and Teslin paper. (g) Absolute resistances of the CNT/Au hybrid electrode *vs.* electrode width. (h) Absolute resistance changes of the CNT/Au hybrid electrodes under different bending angles. Inset: Lighting of LEDs by the Teslin paper with CNT/Au electrodes (bent into "flower" shapes).

and integrated circuits, offering a complementary methodology to commercial flexible printed circuits (Table S1, ESI†).

Photo images of the fabricated regular paper modules (TENG, PMC, MSCs, and FC modules) are exhibited in Fig. 1(c)–(e). Robust Teslin paper is selected as the standard substrate due to its high modulus and fracture resistance (Table S2, ESI†); successively deposited carbon nanotubes (CNTs) and Au thin films (CNT/Au hybrid electrodes) are used as the common electrodes/interconnections/current collectors to ensure excellent conductivity (Fig. S1, S2 and Table S3, ESI†). To prepare the paper modules, we adopt a laser engraving process to pattern the electrodes and interconnections, as it is time-efficient, customizable, scalable with high throughput/resolution, and free from photoresists (Fig. S3a, ESI†). Then, the basic electronic elements (*e.g.*, rectifier bridge, capacitor, inductor, and microcontroller unit (MCU)) are precisely assembled and sintered at desired interconnections on the Teslin paper (Fig. S3b, ESI†). As the circuit layouts for TENG, PMC, and MSC modules are simple and standardized, they can be patterned on a large-area paper substrate in one step and prepared for usage after tailoring (Fig. S3c and Video S1, ESI†). Electrode layouts for the functional circuits are individually designed depending on the demanded applications (Video S2, ESI† shows the example of laser engraving the circuit for flowing LEDs).

Fig. 1(f) shows cross-sectional scanning electron microscopy (SEM) image of the patterned CNT/Au hybrid electrodes on a Teslin paper substrate (the thickness of the Teslin paper and hybrid electrode are 270 and 13 μm, respectively). Excellent conductivity of

the electrodes is a critical requirement for the functional paper modules to implement its integral function. The resistance of the patterned CNT/Au hybrid electrodes is closely related to two parameters: the width of the hybrid electrode (in the same length) and the thickness of the top-deposited Au layer (40, 60, and 80 nm). As shown in Fig. 1(g), the absolute resistances of all the control samples show a decreasing tendency with increasing electrode width. The extracted absolute resistance for pure CNT electrodes is 31.2 kΩ at a width of 0.2 mm and 784 Ω at a width of 5 mm. Although the resistance of CNT electrodes drops by two orders of magnitude with increasing width, it is still too high to be directly used as an interconnection for electronic elements. Depositing Au layers (good conductor) on CNT films can effectively decrease the resistance of the as-prepared hybrid electrodes (<10 Ω). According to the comprehensive evaluation of absolute resistance and specific density, we reasonably select CNT/Au-60 (deposited Au layer at 60 nm) as the standard electrodes for the sustainable paper modules (Fig. S4a, ESI†). CNT/Au-60 hybrid electrodes are also demonstrated with excellent flexibility, as shown in Fig. 1(h). With the bending angle of the paper-based electrode (2 mm width) changed from -180° to 180° (*i.e.*, from bending outward to bending inward), the absolute resistance shows negligible variations (14 to 19 Ω), which ensures the durability of hybrid CNT/Au-60 electrodes for potential robust applications of the paper module. Insets indicate that the LED belts constructed on the curved hybrid electrodes (assembled into two "flower" shapes) are capable of working well. Lighting the LEDs on circumvolute or wavy paper electrodes is also available with hybrid electrodes of larger length (10 cm, Fig. S4b, ESI†).

2.2 Paper-TENG as the power source

To achieve the sustainability of the functional paper modules, paper-based local and adaptive power sources are the primary choice. TENGs, relying on contact-electrification and electrostatic-induction, can effectively harvest mechanical energy from surrounding environments.[50] Facile contact-separation motion between two different materials can induce impressive alternating outputs, which promises TENGs with abundant materials choices in low cost and light weight. Furthermore, TENGs can be readily fabricated on various paper substrates[51] or designed/embedded in Origami/Kirigami structures.[52] Regarding the excellent bending-elastic properties of the adopted Teslin paper substrate, a facile but efficient paper-TENG designed in folio-shape (contact-separation mode) is utilized as the power source for the sustainable paper modules. The two conductive layers for the folio-shaped paper-TENG are the forementioned CNT/Au-60 hybrid electrodes (patterned by a laser engraving process in one-step together with electrodes for other modules), while the friction layer is a commercial fluorinated ethylene propylene (FEP) film attached to the bottom electrode. The working mechanism of the paper-TENG for generating electricity can be explained in four consecutive steps in a full contact-separation cycle (Fig. 2(a)). In the original contact state, negative electrostatic charges are induced on the surface of the FEP, while positive charges are gathered on the top CNT/Au hybrid electrode according to the contact electrification effect. The whole TENG device is in a charge neutralization state due to the electrostatic equilibrium, exhibiting no output current. Once the top CNT/Au electrode is released from the bottom FEP friction layer, the induced opposite electrostatic charges cannot be neutralized with each other. The electrons gathered at the FEP surface lose constraints and start to flow from the bottom CNT/Au electrode to the top electrode through an external load circuit, driven by the induced triboelectric potential. Further separation between the FEP and top CNT/Au electrode will enhance the triboelectric potential to a maximum value at the largest separation state. When the paper-TENG is compressed back to the original state, the induced triboelectric potential will decrease gradually, which drives electrons to flow back and induces a current output in the reversed direction. The induced triboelectric potential distributions can be readily simulated by COMSOL employing finite element analysis (Fig. 2(b)). Upon contact-separation distance at 6 cm, the induced triboelectric potential in the paper-TENG (conformal area at 5×5 cm^2) is simulated to be able to reach a maximum value of 850 V. When the frequency of periodic contact-separation motions is increased from 1 to 5 Hz, the open-circuit voltage (V_{OC}) of the paper-TENG gradually increases from 600 to 836 V (Fig. 2(c)). Similarly, the short-circuit current (I_{SC}) also presents an incremental trend with increasing frequency, changing from 48 μA at 1 Hz to 120 μA at 5 Hz. The corresponding transferred charges (Q_{SC}) under different contact-separation frequencies have no significant changes (maintained at $\sim$300 nC). The variation tendency of V_{OC}, I_{SC}, and Q_{SC} can be explained from the Gauss theorem and Maxwell's displacement current (Supplementary Note 1, ESI†). The corresponding real-time I_{SC} and V_{OC} after rectification (Fig. S5a, ESI†) and over 10 000 cyclic tests (Fig. S5b, ESI†) also indicate the excellent stability and robustness of the paper-TENG.

To evaluate the power density of the paper-TENG, the output currents are characterized by connecting different load resistors. As displayed in Fig. 2(d), the output current value drops with increased load resistance owing to the Ohmic law, while the instantaneous peak power ($P = {I_{peak}}^2 R$) is maximized to a peak power density ($P_S = \frac{{I_{peak}}^2 R}{S}$) of 3.25 W m^{-2} with a load resistance of 100 MΩ. The standard charging capacity of the paper-TENG is characterized by using it to charge commercial capacitors (2.2, 10, 33, and 100 μF). As plotted in Fig. 2(e), it takes 675 s to charge the capacitor of 100 μF to 10 V, but it only takes 19 s to charge the 2.2 μF capacitor to 10 V. Moreover, without any rectification or power management, the prepared paper-TENG (5×5 cm^2) with intrinsic AC outputs can be directly used to light up 44 LEDs in flashing state (series connected in a "BINN" shape, Fig. 2(f)). The above results indicate that the paper-TENG can easily harvest regular mechanical energy and is qualified to work as a reliable power source for sustainable paper modules.

2.3 Paper-based MSCs for energy storage module

The paper-based energy storage module is demonstrated with typical miniaturized electrochemical devices (MSCs), which have the advantages of excellent rate capability, fast charging/discharging ability, high power output, mechanical robustness,

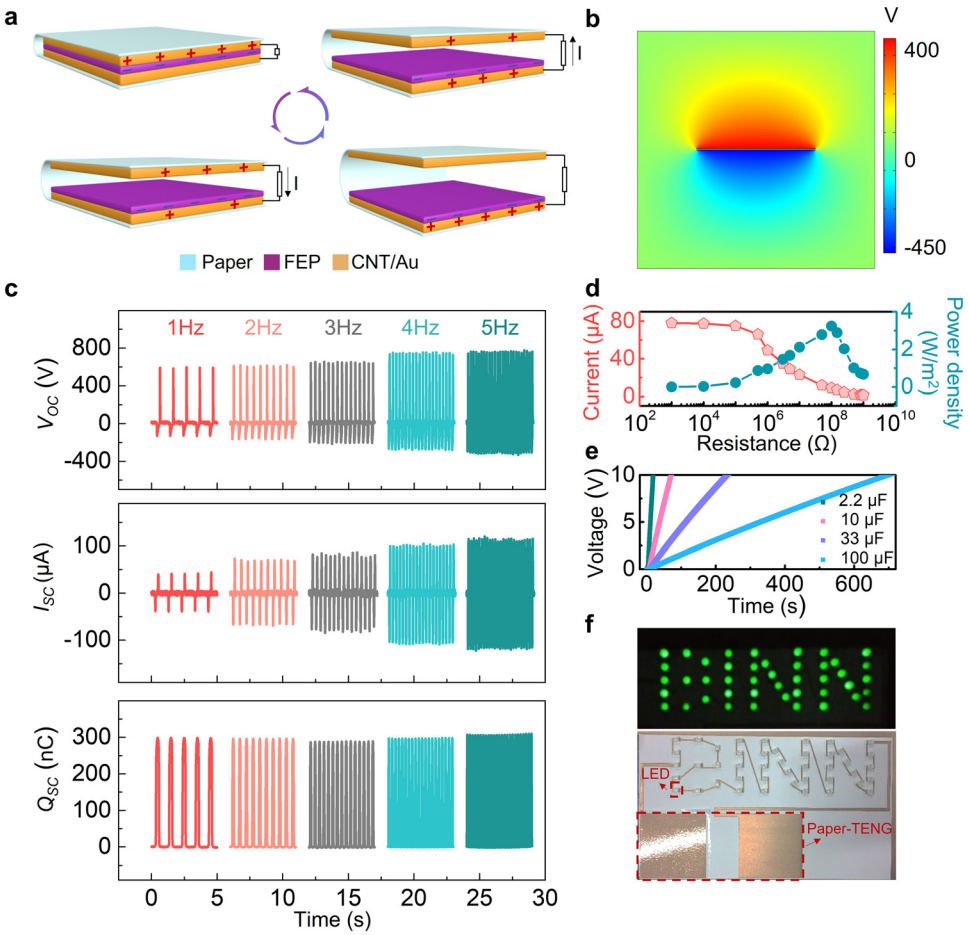

Fig. 2 Working principle and output characteristics of the paper-TENG module. (a) Schematic diagram of the working principle for the paper-TENG in contact-separation mode. (b) COMSOL simulation for the triboelectric potential in the paper-TENG. (c) Electrical outputs (V_{OC}, I_{SC}, and Q_{SC}) of the paper-TENG under different contact-separation frequencies (1–5 Hz). (d) Dependence of the TENG output current and power density on different load resistances. (e) Charging commercial capacitors by the paper-TENG. (f) Lighting up 44 LEDs in series connection in a "BINN" shape by the paper-TENG (5×5 cm^2).

and facile on-chip integration opportunities. The intrinsic planar electrode structures in MSCs are especially compatible with the adopted laser-engraving technique, which is beneficial for scalable fabrication in high throughput. Fig. 3(a) shows a photo of the MSC module with interdigital CNT/Au hybrid electrodes patterned in a length of 10 mm, a width of 0.3 mm, and an interspacing distance of 0.4 mm (SEM image in Fig. S6, ESI†). As the active electrode materials, the deposited CNTs featuring randomly entangled/crosslinked fibrous morphology (Fig. S1b, ESI†) exhibit a high specific surface area that can facilitate charge accumulation at the electrode and electrolyte interface (crucial for electrical-double-layer capacitive electrode material, Fig. S7, ESI†). The surface roughness and microporous structures are also ideal for electron and ion transport across the entire interdigital structure (especially inside the electrode), which is beneficial to fully utilize the electrode materials and achieve excellent capacitive performance. The interdigital hybrid electrodes can be directly used for the paper-based MSC module after covering with solidified H_2SO_4/polyvinyl alcohol (PVA) electrolyte. The electrochemical performances of the prepared paper-based MSCs are systematically and comprehensively characterized. Cyclic voltammetry (CV) curves are firstly investigated at ordinary scan rates from 10 to 100 mV s^{-1} (Fig. 3(b)) and at fast scan rates from 1 to 10 V s^{-1} (Fig. 3(c)). The MSCs exhibit an exceptionally enhanced electrochemical performance with a near-perfect rectangular shape in the CV curves (even at high scan rates from 1 to 10 V s^{-1}), indicating typical electrical-double-layer capacitive behavior. According to the galvanostatic charging/discharging (GCD) tests at a discharging current density of 2 μA cm^{-2}, the extracted maximum areal specific capacitance of the MSC is calculated to be ~1.6 mF cm^{-2}. When the discharging current density is increased to 20 μA cm^{-2}, the areal specific capacitance can remain at 90.5% (only shows a slight decrement with increased charging/discharging current density, Fig. 3(d)). A symmetric triangular shape is observed from the GCD curves, and no obvious voltage drop is observed at the beginning of each discharging plot (inset of Fig. 3(d)), which indicates an excellent and reversible capacitive property with good electrical conductivity of CNT/Au hybrid electrodes. The achieved maximum areal

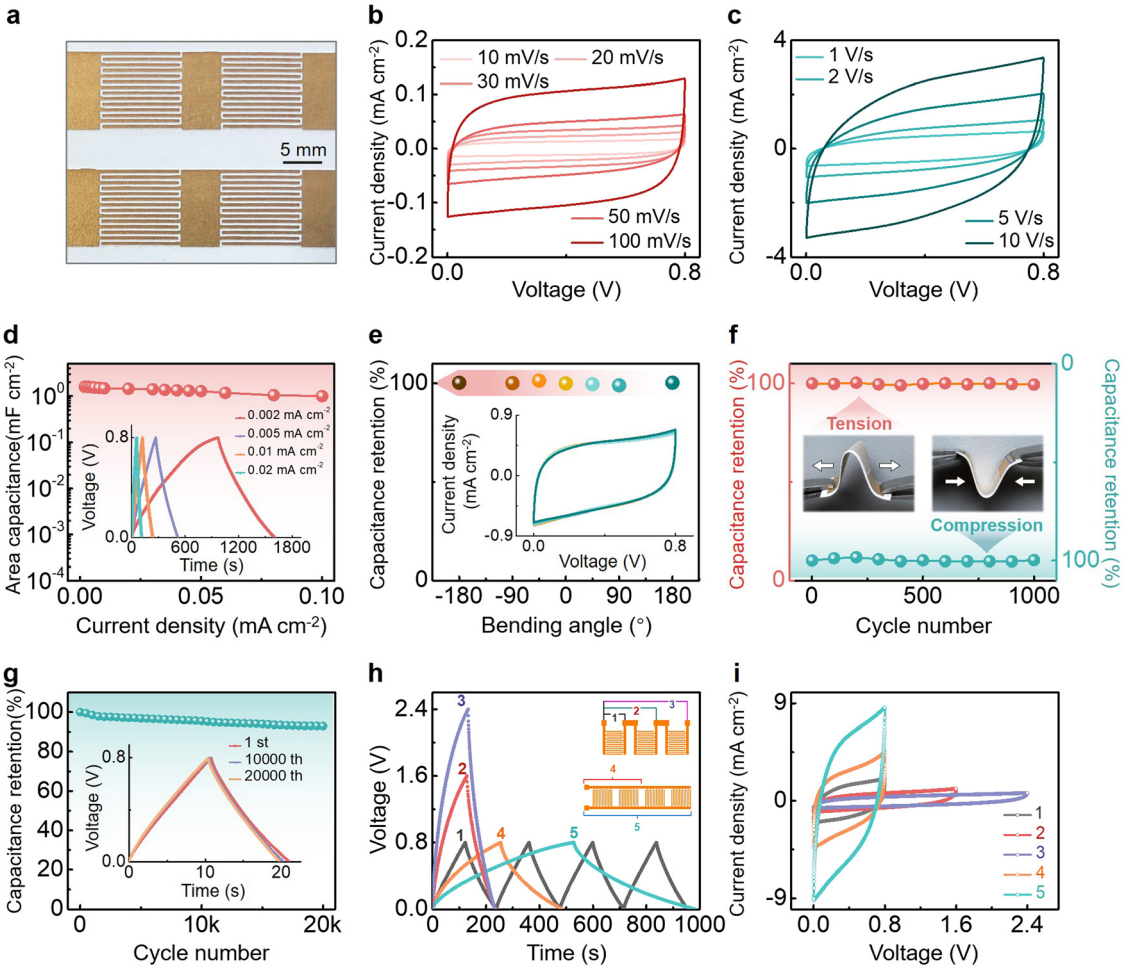

Fig. 3 Electrochemical characteristics and mechanical flexibility of the MSC paper module. (a) Photo image of the interdigital MSCs. Cyclic voltammetry (CV) curves of MSCs obtained at (b) slow scan rates of 10–100 mV s^{-1} and (c) fast scan rates of 1–10 V s^{-1}. (d) Rate capacity of the paper-based MSCs. The inset shows the galvanostatic charge/discharge (GCD) curves at different current densities. (e) Capacitance retention of the MSCs under different bending angles. Insets are CV curves obtained at 1 V s^{-1}. (f) Capacitance retention of the MSCs after 1000 cycles of charging/discharging under both tensile/compression states. Insets are the photo images of MSC paper module under tensile/compression states. (g) Cyclic stability of the MSC module. Insets are the GCD curves for the MSC after 10 000 and 20 000 cycles at a current density of 0.08 mA cm^{-2}. (h) GCD curves (current density = 0.01 mA cm^{-2}) and (i) CV curves (scan rate = 5 V s^{-1}) for the MSCs connected in parallel and in series.

specific capacitance of the paper MSC module (1.6 mF cm^{-2}) is comparable to that of recently reported MSCs with carbon active materials, such as multilayered graphene (62.7 μF cm^{-2}),[53] graphene ink (1 mF cm^{-2}),[54] porous nanostructured carbon films (666 μF cm^{-2}),[55] *etc.* The corresponding Nyquist plots of the paper-based MSCs are explained in Fig. S8a (ESI†).

To identify the flexibility of the paper-based MSCs, CV curves of the MSC module are also tested at different bending angles. As shown in Fig. 3(e), no obvious capacitance decrement can be observed with the MSC bending at different angles (−180° to 180°), confirming its extraordinary bendability. The CV curves also overlap well (inset of Fig. 3(e)), further suggesting the high robustness and stability of the paper-based MSC module. The capacitance retention tests under 1000 cycles of repeated tensile and compressive bending at 180° also exhibit no significant changes, indicating excellent mechanical stability and robust flexibility (Fig. 3(f), insets are the photo images of two opposite bending states). The CV curves at a high scan rate of 1 V s^{-1} in different cycles can still maintain almost the same shape, as shown in Fig. S8b (ESI†). In addition, the stable cycling performance of the MSC is shown in Fig. 3(g). The capacitance retention can be readily maintained at ~93% after being charged/discharged at 0.08 mA cm^{-2} for 20 000 cycles, implying no significant differences in the capacitive behaviors during the cyclic charging/discharging process. The adopted laser-engraving process is also ready to pattern MSCs in different connection styles (in series or in parallel connections), which is available to certain applications that require higher current or voltage. Series connections of two or three MSCs can easily widen the voltage window to 1.6 or 2.4 V, while the parallel connection can maintain the voltage window unchanged but increase the discharging time (Fig. 3(h)). Parallel connection of the MSCs also increase the output current density (Fig. 3(i)). The paper-based MSCs in series/parallel can be readily

prepared by the laser-engraving technique (processing within several seconds), which can also effectively avoid cumbersome current collectors or external interconnects.

2.4 Paper module of the power management circuit

The TENG device is ready to harvest mechanical energy from various mechanical motions at variable frequencies, commonly exhibiting regular high-voltage and low-current output characteristics. Due to the intrinsic pulsed alternating-current (AC) outputs, high inherent impedance, and large impedance mismatch (between TENGs and electronic devices), a regular TENG is inefficient at directly powering (or charging) electronic devices. To work as the power source for the functional paper modules (or charging energy storage units) which generally requires high-current and low-voltage, a paired power management module is critical to realize efficient energy utilization from the intrinsic pulsed outputs by the paper-TENG. To achieve the power management module for the sustainable operation, a necessary power management circuit is designed on Teslin paper to implement DC buck conversion and maximize the energy conversion in a self-management strategy. Fig. 4(a) shows a photo of the PMC paper module, which is composed of a low-loss full-wave rectifier bridge, three capacitors, a standard high-efficiency buck converter, and one inductor. By integrating these key components, the PMC paper module is achieved and optimized to form a complete energy harvesting solution for power sources with high output impendence (here is the paper-TENG). The PMC works in an ultralow quiescent current undervoltage lockout (UVLO) mode with a wide hysteresis window, which allows charges to accumulate on the input capacitor until the buck converter can efficiently

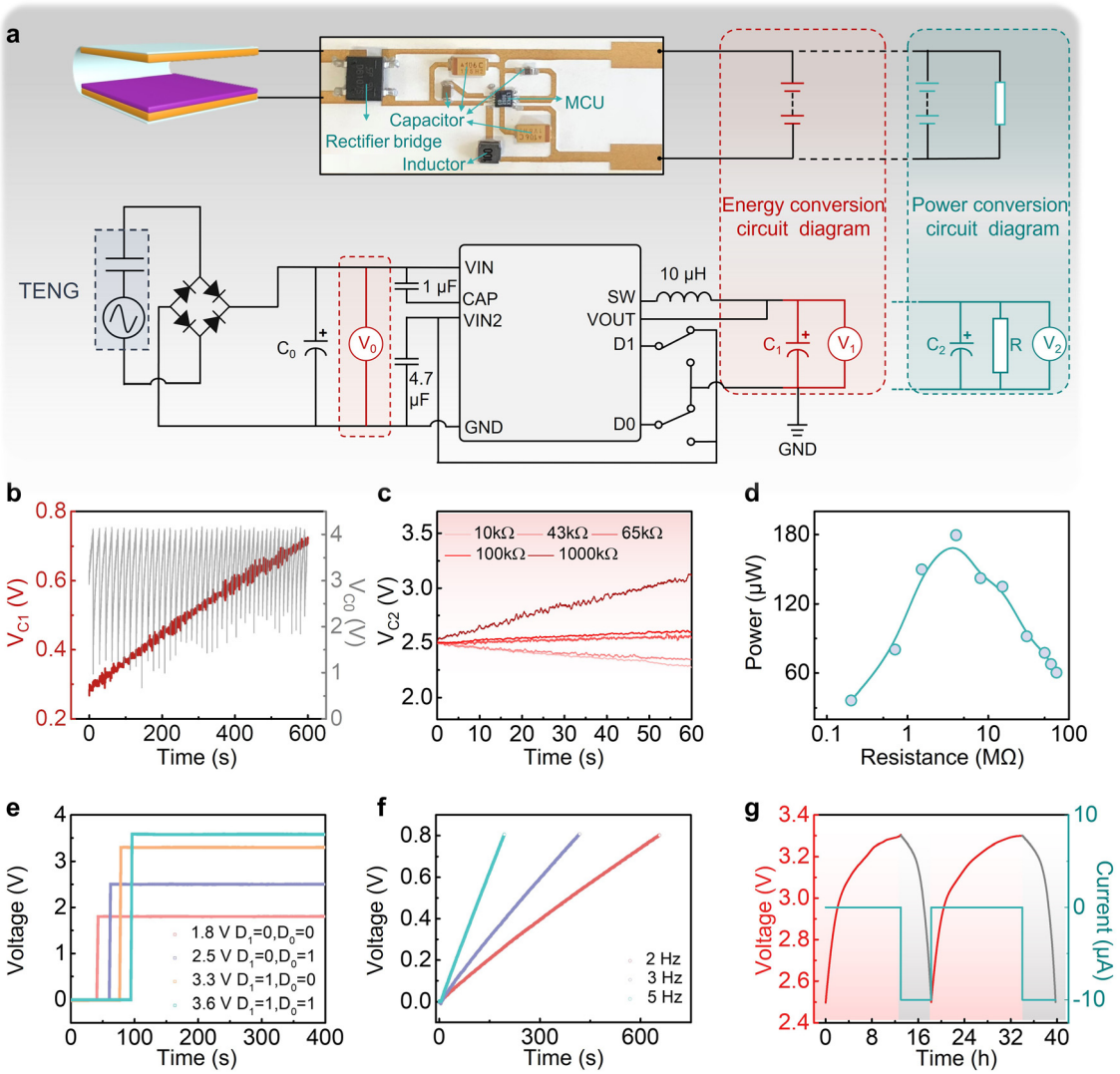

Fig. 4 Schematic illustration and working principle of the PMC paper module. (a) Photo image and circuit diagram of the PMC paper module. (b) Measurement of the energy transfer efficiency. (c) Measurement of the power transfer efficiency. (d) Maximum power of the paper-TENG under palm tapping. (e) Four typical DC outputs based on the PMC paper module. (f) Charging curves for paper-based MSC by paper-TENG through the PMC module (under contact-separation frequency of 2, 3, and 5 Hz). (g) Charging/discharging curves for lithium-ion battery by paper-TENG though the PMC paper module.

transfer a portion of the stored charges to the output. A circuit diagram of the PMC paper module is shown in the bottom panel of Fig. 4(a) (details in Fig. S9, ESI†). A 1 μF capacitor is connected between V_{IN} and CAP (CAP is an internal rail referenced to V_{IN}, the gate driver for buck switch) and a 4.7 μF capacitor is connected between V_{IN2} and GND (grounding pin). The buck is optimized to work with an inductor in the range of 10 to 22 μH. The low-loss full-wave bridge rectifier is used to rectify the intrinsic AC output signals from the paper-TENG and prevent electrons from being fed back to the energy-harvesting source. The generated electrons are gradually delivered to charge the input capacitor (C_0) during the energy-harvesting process. When the voltage on V_{IN} is monitored to rise above the UVLO rising threshold, the buck converter is enabled to work, and the charges will be transferred from the input capacitor (C_0) to the output capacitor (C_1). Then, the buck converter can efficiently transfer energy stored at a high voltage to a regulated/programmed output (V_{OUT}) to the external load (an electronic device or energy storage device). Notably, the designed PMC paper module is capable of directly interacting with the AC power source of the paper-TENG, rectifying the voltage waveform to store the harvested energy on an external capacitor, and maintaining a regulated output voltage by means of a high efficiency synchronous buck regulator (detailed working mechanism in Fig. S9, ESI†).

To evaluate the performance of the PMC paper module, two back-end circuits are designed to characterize the energy and power conversion efficiency (circuits in the right part of Fig. 4(a)). The energy conversion efficiency is evaluated through the circuit in which a storage capacitor (C_1) is connected in series with the output terminal of the buck converter (red frame in Fig. 4(a)), while the power conversion efficiency is evaluated through the circuit in which a load resistor (R) is additionally connected in parallel with the storage capacitor C_2 (cyan frame in Fig. 4(a)). By comparing the energy stored in the input capacitor (C_0) directly charged by the TENG, the energy transfer performance of the PMC paper module can be evaluated by the energy conversion efficiency (η_E), which is defined as the ratio of the energy stored in C_1 (E_{c1}) to the total energy transferred out from C_0 (E_{c0}). The real-time capacitance changes of C_0 and C_1 in the PMC paper module are monitored during the mechanical energy scavenging process through hand-tapping on the paper-TENG. C_0 is first charged by the paper-TENG *via* the rectifier bridge. When the voltage of C_0 is charged to reach 4 V (rise above the UVLO rising threshold), the buck converter is activated to allow the accumulated and stored charges in C_0 to release/transfer to C_1 through the buck circuit. This process leads the voltage of C_1 to increase stepwise and results in a gradually decreasing voltage of C_0 (Fig. 4(b)). Within 600 s, C_0 (capacitance is 1 μF) is charged and discharged for 42 times, and the released energy is evaluated to be 276 μJ. Meanwhile, the voltage across C_1 (capacitance is 1.1 mF) is increased from 0.23 to 0.71 V, and the corresponding charging energy is calculated to be 245.5 μJ. Accordingly, the energy conversion efficiency of the PMC module defined by E_{C1}/E_{C0} is 88.9% (Supplementary Note 2, ESI†).

Another important figure of merit for the PMC module is the power management efficiency (η_P), which is defined as the ratio between the power stored in C_2 and the total power generated from the TENG. The power conversion circuit (cyan frame in Fig. 4(a)) includes a parallel load resistor R with C_2, in which C_2 is charged by the front-end energy conversion circuit and the potential drop at R is monitored (*i.e.*, the charged voltage V_{C_2} in capacitor C_2). To characterize the power management efficiency η_P, we also use the paper-TENG directly driven by palm tapping as the power source and measure the power delivered to the load R after management by the PMC paper module. As shown in Fig. 4(c), the available charged voltage V_{C_2} for C_2 is monitored in real time with the parallel connected R at different resistance values. V_{C_2} shows a positive slope with a larger R (100 and 1000 kΩ), which indicates that the power consumption of the load resistor R is lower than the power provided by the paper-TENG in this case. This is because a larger resistance value of the load resistor R hinders electrons from flowing and leads to a higher efficiency of charge accumulation and storage in C_2 (thereby leading to a V_{C_2} increment with time). With the load R at smaller resistance values (10, 43, and 65 kΩ), the slope of the V_{C_2}–t curve shows a tendency to become more negative, indicating the power delivered from palm tapping is not enough to compensate for the energy consumption on the external load. Notably, the slope of the charging curve changes to 0 with R = 65 kΩ, which means the power delivered from C_2 is equal to the power consumption on the load R (denoted as $P_{C_2,max}$). In this case, the consumed power is the maximum power delivered to the resistive load after power management, which is calculated to be 96.2 μW. The maximum power generated from the power source of the paper-TENG under palm tapping ($P_{TENG,max}$) is evaluated to be 179.6 μW (Fig. 4(d), extracted from Fig. S10, ESI†). Accordingly, the critical power management efficiency for the PMC module defined by $P_{C2,max}/P_{TENG,max}$ is 53.6% (Supplementary Note 3, ESI†).

Based on the PMC paper module, the intrinsic high-voltage and pulse output of the paper-TENG can be successfully converted into stable outputs at the V_{OUT} terminal in four selectable values (1.8, 2.5, 3.3, and 3.6 V, Fig. 4(e)). Through the PMC module, the energy storage paper module (paper-based MSCs) is capable of being charged by the paper-TENG under different contact-separation frequencies (2–5 Hz, Fig. 4(f)). The charging rate increases with increasing contact-separation frequency. The paper MSC can be charged to 0.8 V within 200 s at a contact-separation frequency of 5 Hz. As shown in Fig. S11 (ESI†), eight paper-based MSCs in series are also demonstrated to be successfully charged and reconnected in parallel to power an LED. Furthermore, as shown in Fig. 4(g), the commercial lithium-ion battery (LIB) can also be charged by the paper-TENG through the PMC paper module, which takes ~13 h to be charged from 2.5 to 3.3 V (one of the standard output voltages to power basic electrical appliances). The charged LIB can be used for 6 h according to the discharge curve from 3.3 to 2.5 V at a current load of 10 μA. The demonstrated PMC paper module is capable of implementing successful power management for more effective charging applications, which is of great significance for the terminal paper module to function well.

2.5 Sustainable functional paper modules

Paper-TENG, PMCs, and energy storage units constitute the energy supply part of the functional paper modules (Fig. 5(a)), which are critical to its sustainability and energy-autonomy. Paper-TENGs with high-impedance are ready to harvest ubiquitous mechanical energy in the ambient environment; the PMC paper module is paired with a high-output-impedance energy source to optimize the energy conversion efficiency; and paper-based MSCs are assembled for efficient energy storage and broad applications. Each of the paper modules has its specific function and can be used individually, incorporated (to drive high-power-consuming electronics), or replaced/selected depending on different circumstances. As a complete prototype of paper-based sustainable modules, functional circuits and devices are also required to be capable of implementing the terminal function on paper substrates, *i.e.*, functional paper modules. We have demonstrated three typical functional circuits on Teslin paper, including flowing LEDs, temperature/humidity sensors, and infrared (IR) wireless emitters/controllers. As the demonstrated functional circuits need to be driven by the programmed

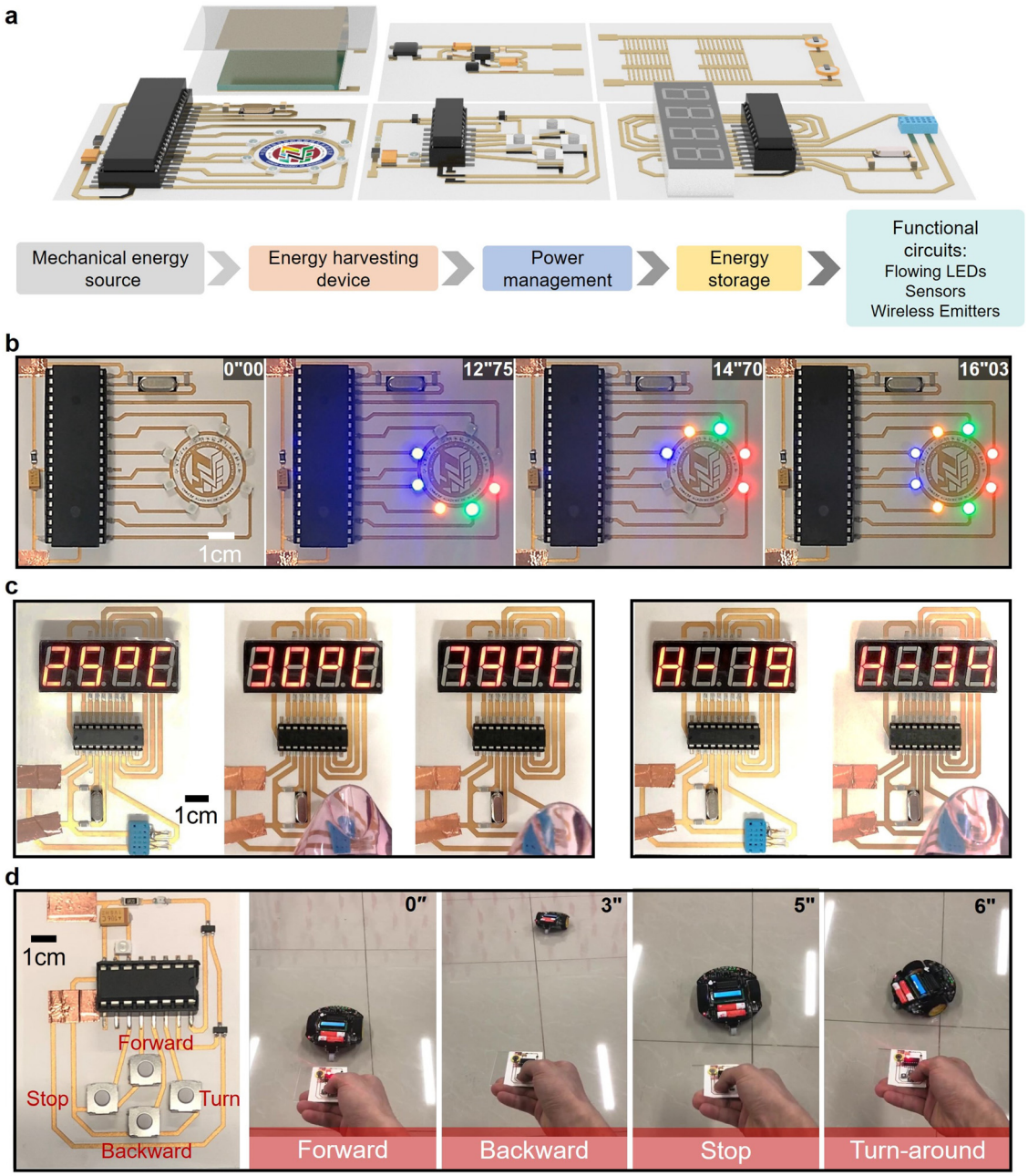

Fig. 5 Operation of the paper module for different functional circuits. (a) Schematic illustration of the energy autonomous paper modules and functional circuits. Operation of the functional paper module for (b) flowing LEDs, (c) temperature/humidity sensor, and (d) IR remote controller for a playmobile. The scale bar is 1 cm.

MCU (the required operating voltage at ~5 V), two LIBs charged by the paper power modules are used to drive each functional paper module.

Fig. 5(b) displays the first functional paper module of the flowing LED circuit, which includes an MCU (with an embedded program as the core to drive the flashing process of the eight LEDs) and other necessary components of three capacitors, two resistors, and a crystal oscillator (Fig. S12a, ESI†). According to the circuit diagram in Fig. S12b (ESI†), it comprises a clocking circuit, a reset circuit and a flowing LED circuit. The clock circuit adopts a 12 MHz crystal oscillator paired with two 20 pF capacitors to provide the time reference for the implementation of the program commands in the internal circuitry of the MCU, in strict accordance with the timing sequence. The working modes of paper-based flowing LEDs can be readily designed according to the embedded programs. The corresponding operation process (including three stages) is shown in Fig. 5(b) and Video S3 (ESI†). At the first operation stage, the eight LEDs are turned on and off sequentially in the clockwise direction (two cycles with time from 0–11.07 s); the second stage is when five LEDs are lighted up and held for a while from 12.75 to 14.70 s, and the remaining three LEDs are in the off-state until all eight LED lights up until 16.03 s; the third stage is to turn off three LEDs and light up these three LEDs in turn until all the LEDs are finally turned off. The operation time for the first cycle of the flowing LED circuit is ~1 min, and the next cycle will be carried out after the first cycle is completed.

The second functional paper module demonstrates the functional circuit of a typical DHT12 digital temperature/humidity sensor, which is successfully designed and replicated on the Teslin paper substrate (Fig. 5(c)). The DHT12 digital temperature/humidity sensor is a standardized temperature/humidity sensor containing a calibrated digital signal output, which is ultrasmall, low-power-consuming, and suitable for a variety of applications. The paper-based DHT12 digital temperature/humidity sensor contains the basic electronic elements of an integrated temperature/humidity sensor, a crystal oscillator, an MCU, and a four-digit segment display (Fig. S13a, ESI† circuit diagram in Fig S13b, ESI†). The four-digit segment display can indicate the temperature and humidity in real time (Fig. 5(c) and Video S4, ESI†). For instance, the relative humidity of the ambient environment at the test moment is 19%, and the temperature is 25 °C. After heating with a hair dryer, the changes in the detected temperature (30 °C and 79 °C) and relative humidity (H-34) are shown on the segment display.

Fig. 5(d) shows the demonstrated functional paper module of an IR remote controller for a playmobile, which includes the key components of a resistor, a capacitor, a triode, an MCU, and four switches (S1–S4) for direction control (Fig. S14, ESI†). The MCU is controlled by a wireless transmitting/receiving module to translate/transmit instructions for the corresponding function of remote control. When we press the switch in sequence (from S1 to S4), the IR-emitter paper module can send out a series of binary pulse codes (*i.e.*, IR signals with high/low level conversions according to certain timing rules) to the target IR receiver on the playmobile. Subsequently, the IR receiver on the playmobile decodes the transmitted signal to deliver the movement instructions to the playmobile (moving forward/backward, stop, and turn-around). Thus, the playmobile can be readily remote-controlled to move on commands as shown in Video S5 (ESI†) (photo images of moving forward (0″), backward (3″), stop (5″), and left and right turn (6″) in Fig. 5(d)). All the above demonstrated paper-based functional circuits represent the excellent availability, reliability, and integratability of the sustainable functional paper modules in an energy-autonomous fashion (Fig. S15 and Table S4, ESI†).

3. Conclusions

In summary, we have successfully demonstrated the prototype of sustainable functional paper modules, which comprise TENG energy harvester, power management component, energy storage units, and functional circuits. The modular layout for the paper-based functional circuits is unified and compatible with a scalable and time-efficient laser-engraving technique. The demonstrated functional paper modules can readily harvest (bio)mechanical energy through the paper-TENG (power density of 3.25 W m^{-2}); the designed PMC component can effectively regulate the TENG AC input into a steady and continuous DC output for improving the charging/powering efficiency (energy and power conversion efficiency is 88.9% and 53.6%); the integrated paper-based MSCs represent excellent rate capacity (specific capacitance remains 90.5% at 20 μA cm^{-2}), mechanical stability (over 1000 bending), and retention performance (over 20 000 cyclic tests); and finally the paper-based functional circuits are successfully demonstrated with modular functions of flowing LEDs, temperature/humidity sensors, and IR remote controllers. Benefiting from the modular design, the sustainable paper modules are capable of working individually or integrated to implement specific applications (with selected paper modules). In addition, the working process of the functional paper modules embodies an energy circulation of energy harvesting, management, storage, and application, which further manifests the sustainable characteristics from the aspect of energy form.

The demonstrated sustainable functional paper modules offer new paradigm for energy autonomous systems, which will lead future R & D trends toward device innovation, technology revolution, and system integration from the following aspects.

(1) Structure design. Teslin paper utilized as the body material is foldable, tailorable, and designable in arbitrary shape, which is highly promising to extend the sustainable paper modules to sophisticated stretchable or three-dimensional counterparts by introducing Kirigami or Origami designs. Corresponding topological electrode layouts paired with proper conductive materials and processing techniques (compatible with paper electronics) are believed to broaden more realistic applications with higher spatial efficiency.

(2) Materials development. Optimizing the active materials for energy harvesters and energy storage devices on the Teslin paper substrate can further improve the performance of related

paper modules for a wider range of functional electronics. Besides, the elaborate selection of resistive, capacitive, and inductive materials with compatible processing on paper substrate can help to remove the commercial rigid electronic elements (*e.g.*, resistor, capacitor, inductor). Further development on high-performance semiconductor channel materials (for transistors, memories, logic circuits, and microprocessors) or active sensing materials (for environmental or physiological sensors) paired with current processing techniques in paper industry is also highly encouraged to deliver potential logic functional and processing ability to the paper modules, which may help to further replace the logic/processing components (*e.g.*, MCUs) and facilitate fully flexible paper modules.

(3) Power sources. Optional energy harvesting devices with complementary characteristics (*e.g.*, piezoelectric/pyroelectric/triboelectric nanogenerators, photovoltaic/biofuel cells, or hybrid energy harvesters) are extensively available for sustainable paper modules to improve the energy supply efficiency.

(4) Manufacture process. The possibility to integrate various functional devices and circuits within the production lines of the paper industry has always been of great significances to enhance (or add) new functionalities to conventional paper-based electronics. Relevant manufacturing strategy or hybrid processing methods (*e.g.*, laser engraving, ink-jet printing, reel-to-reel patterning, soft lithographical techniques) should be developed for cheap and mass production of functional paper modules.

The proposed prototype of sustainable paper-based functional circuits with modular design principles in this work is expected to promote the fast development of modularized, integratable, and customizable consumer electronics with multiple functions and energy autonomy.

Experimental section

Preparation of CNT/Au hybrid electrodes

First, 5 ml of the CNT ink (TNHC-2) was poured evenly on the Teslin composite paper (SP1400). The CNT ink was scraped evenly across the composite paper with a glass rod, and then the processed Teslin paper was dried in an oven at 50 °C for 20 min. Second, the composite paper with CNTs was placed into a magnetron sputtering chamber (Discovery 635), and the Au electrode was sputtered onto the surface of the composite paper with CNTs (sputtering for 10 min). Thus, the CNT/Au hybrid electrodes on Teslin paper were obtained.

Fabrication of MSC paper module

First, the interdigital electrode patterns for MSCs were drawn with CorelDraw software, which could be recognized by the laser engraving equipment (LM-9060) to conduct a relevant lase-engraving process for the CNT/Au electrodes. Second, to prepare the PVA/H_2SO_4 gel electrolyte, PVA solution was prepared by dissolving 5 g of PVA (molecular mass = 89 000–98 000) in 20 mL of deionized (DI) water (with subsequent heating and stirring at 90 °C for 1 h); 5 mL of H_2SO_4 was added dropwise to 30 mL of DI water; and the diluted H_2SO_4 was then added slowly into the PVA solution. After cooling to room temperature, the PVA/H_2SO_4 gel electrolyte was obtained. Finally, the PVA/H_2SO_4 gel electrolyte was evenly coated on the interdigital CNT/Au electrodes, followed by a subsequent dehydration process in a vacuum oven for 15 min. The coating and heating processes were repeated three times to finally achieve the paper-based MSCs.

Fabrication of functional circuits module

A circuit diagram for the functional module is drawn with CorelDraw software and corresponding CNT/Au electrode patterns are prepared by the laser engraving process. Then, the electronic components are accurately pasted/sintered onto the interconnections assisted with solder paste. After removing the solvent and additives by a heat gun, the electronic components can be soldered together with the electrodes to form a permanent connection.

Simulation of triboelectric potential

COMSOL Multiphysics is utilized to simulate the electrical potential of the paper-TENG in contact-separation mode. Firstly, we choose the two-dimensional mode (spatial dimension) to simulate the electric field and electrical potential of the paper-TENG by selecting the electrostatic mode of AC/DC in the physical field and presetting the steady state. Then, we set Component 1 in rectangle shape (5 × 5 cm^2, material of Au) as the positive triboelectric layer, and set Component 2 in rectangle shape (5 × 5 cm^2, material of FEP) as the negative triboelectric layer. Then we set the surrounding environment as Component 3 in large area (25 × 25 cm^2, material of air) to fully cover component 1 and component 2. Afterwards, the electrostatic parameters are set as follows one by one: (1) choosing the grounding boundary of all the four sides of component 3; (2) choosing the suspension potential of all the four sides of component 1; (3) choosing the surface charge density of component 1 and corresponding boundary of component 2. Finally, after setting up all the parameters, the simulation process is conducted and the potential difference between the two friction layers of the paper-TENG is obtained as shown in Fig. 2(b).

Characterizations

To measure the electrical output of the paper-TENG, contact-separation action was applied by using a commercial linear mechanical motor (TSMV120-1S). The short-circuit current and transferred charges were measured by a programmable voltammeter (Keithley 6514). The open-circuit voltage was measured by using an oscilloscope (TBS1104). The electrochemical properties of the MSC module were investigated by using an electrochemical workstation (CHI760E Instruments) to measure the CV, GCD, and Nyquist plots recorded in the frequency range of 0.1 Hz to 100 kHz. The areal specific capacitances (C_S)

calculated from galvanostatic charging/discharging plots were derived according to the following equation:

$$C_S = \frac{I \cdot \Delta t}{\Delta V \cdot S}$$

where I is the discharging current, Δt is the discharging time, ΔV is the potential difference with consideration of the voltage drop, and S is the total area of the interdigital shape.

The surface morphologies and thicknesses of the Teslin paper, CNT, and CNT/Au film were determined by field emission scanning electron microscopy (FESEM, SU-8020, Hitachi).

Author contributions

Q. S. conceived the idea and designed the experiment. J. H. and N. X. developed the devices and conducted the measurements. J. H., N. X., J. Y., Y. W., Y. X., and Y. W. investigated the functional modules and tested the circuits. J. H., N. X., J. Y., Y. W., Z. L. W. and Q. S. analyzed the experimental data. J. H., N. X., J. Y., and Q. S. prepared the figures and drafted the manuscript. Z. L. W. and Q. S. guided the whole project. All the authors discussed the results and commented on the manuscript.

Conflicts of interest

There are no conflicts to declare.

Acknowledgements

This work is supported by the National Key Research and Development Program of China (2021YFB3200304), the National Natural Science Foundation of China (52073031, 52192610), Beijing Nova Program (Z191100001119047, Z211100002121148), Fundamental Research Funds for the Central Universities (E0EG6801X2), and the ''Hundred Talents Program'' of the Chinese Academy of Sciences.

References

1 M. M. Waldrop, *Nature*, 2016, **530**, 144–147.
2 M. Lundstrom, *Science*, 2003, **299**, 210–211.
3 Z. L. Wang, *Adv. Mater.*, 2012, **24**, 4632–4646.
4 W. Fan, Q. He, K. Meng, X. Tan, Z. Zhou, G. Zhang, J. Yang and Z. L. Wang, *Sci. Adv.*, 2020, **6**, eaay2840.
5 J. Han, C. Y. Xu, J. T. Zhang, N. Xu, Y. Xiong, X. L. Cao, Y. C. Liang, L. Zheng, J. Sun, J. Y. Zhai, Q. Sun and Z. L. Wang, *ACS Nano*, 2021, **15**, 1597–1607.
6 Y. Lu, H. Tian, J. Cheng, F. Zhu, B. Liu, S. Wei, L. Ji and Z. L. Wang, *Nat. Commun.*, 2022, **13**, 1401.
7 J. Yu, X. Yang, G. Gao, Y. Xiong, Y. Wang, J. Han, Y. Chen, H. Zhang, Q. Sun and Z. L. Wang, *Sci. Adv.*, 2021, **7**, eabd9117.
8 J. Yu, G. Gao, J. Huang, X. Yang, J. Han, H. Zhang, Y. Chen, C. Zhao, Q. Sun and Z. L. Wang, *Nat. Commun.*, 2021, **12**, 1581.
9 P. A. Merolla, J. V. Arthur, R. Alvarez-Icaza, A. S. Cassidy, J. Sawada, F. Akopyan, B. L. Jackson, N. Imam, C. Guo, Y. Nakamura, B. Brezzo, I. Vo, S. K. Esser, R. Appuswamy, B. Taba, A. Amir, M. D. Flickner, W. P. Risk, R. Manohar and D. S. Modha, *Science*, 2014, **345**, 668–673.
10 Q. Shi, Z. Zhang, T. He, Z. Sun, B. Wang, Y. Feng, X. Shan, B. Salam and C. Lee, *Nat. Commun.*, 2020, **11**, 4609.
11 K. Dong, X. Peng, J. An, A. C. Wang, J. Luo, B. Sun, J. Wang and Z. L. Wang, *Nat. Commun.*, 2020, **11**, 2868.
12 H. Song, G. Luo, Z. Ji, R. Bo, Z. Xue, D. Yan, F. Zhang, K. Bai, J. Liu, X. Cheng, W. Pang, Z. Shen and Y. Zhang, *Sci. Adv.*, 2022, **8**, eabm3785.
13 S. Xu, Y. H. Zhang, L. Jia, K. E. Mathewson, K. I. Jang, J. Kim, H. R. Fu, X. Huang, P. Chava, R. H. Wang, S. Bhole, L. Z. Wang, Y. J. Na, Y. Guan, M. Flavin, Z. S. Han, Y. G. Huang and J. A. Rogers, *Science*, 2014, **344**, 70–74.
14 Y. Yang, X. Wei, N. Zhang, J. Zheng, X. Chen, Q. Wen, X. Luo, C. Y. Lee, X. Liu, X. Zhang, J. Chen, C. Tao, W. Zhang and X. Fan, *Nat. Commun.*, 2021, **12**, 4876.
15 L. Yin, K. N. Kim, J. Lv, F. Tehrani, M. Lin, Z. Lin, J. M. Moon, J. Ma, J. Yu, S. Xu and J. Wang, *Nat. Commun.*, 2021, **12**, 1542.
16 M. D. Han, H. L. Wang, Y. Y. Yang, C. M. Liang, W. B. Bai, Z. Yan, H. B. Li, Y. G. Xue, X. L. Wang, B. Akar, H. B. Zhao, H. W. Luan, J. Lim, I. Kandela, G. A. Ameer, Y. H. Zhang, Y. G. Huang and J. A. Rogers, *Nat. Electron.*, 2019, **2**, 26–35.
17 Z. X. Zhang, Q. F. Shi, T. Y. Y. He, X. G. Guo, B. W. Dong, J. Lee and C. Lee, *Nano Energy*, 2021, **90**, 106517.
18 W. He, C. Wang, H. Wang, M. Jian, W. Lu, X. Liang, X. Zhang, F. Yang and Y. Zhang, *Sci. Adv.*, 2019, **5**, eaax0649.
19 D. Y. Park, D. J. Joe, D. H. Kim, H. Park, J. H. Han, C. K. Jeong, H. Park, J. G. Park, B. Joung and K. J. Lee, *Adv. Mater.*, 2017, **29**, 1702308.
20 M. Zhu, Z. Sun, T. Chen and C. Lee, *Nat. Commun.*, 2021, **12**, 2692.
21 A. Chortos, J. Liu and Z. A. Bao, *Nat. Mater.*, 2016, **15**, 937–950.
22 F. Wen, Z. Zhang, T. He and C. Lee, *Nat. Commun.*, 2021, **12**, 5378.
23 S. Niu, X. Wang, F. Yi, Y. S. Zhou and Z. L. Wang, *Nat. Commun.*, 2015, **6**, 8975.
24 Y. Zi, S. Niu, J. Wang, Z. Wen, W. Tang and Z. L. Wang, *Nat. Commun.*, 2015, **6**, 8376.
25 Y. Zi, J. Wang, S. Wang, S. Li, Z. Wen, H. Guo and Z. L. Wang, *Nat. Commun.*, 2016, **7**, 10987.
26 R. Lin, H. J. Kim, S. Achavananthadith, Z. Xiong, J. K. W. Lee, Y. L. Kong and J. S. Ho, *Nat. Commun.*, 2022, **13**, 2190.
27 L. Manjakkal, L. Yin, A. Nathan, J. Wang and R. Dahiya, *Adv. Mater.*, 2021, **33**, 2100899.
28 R. Lin, H. J. Kim, S. Achavananthadith, S. A. Kurt, S. C. C. Tan, H. Yao, B. C. K. Tee, J. K. W. Lee and J. S. Ho, *Nat. Commun.*, 2020, **11**, 444.
29 H. A. Atwater and A. Polman, *Nat. Mater.*, 2010, **9**, 205–213.
30 Z. L. Wang and J. H. Song, *Science*, 2006, **312**, 242–246.
31 F. R. Fan, L. Lin, G. Zhu, W. Z. Wu, R. Zhang and Z. L. Wang, *Nano Lett.*, 2012, **12**, 3109–3114.

32 S. Hong, Y. Gu, J. K. Seo, J. Wang, P. Liu, Y. S. Meng, S. Xu and R. Chen, *Sci. Adv.*, 2019, **5**, eaaw0536.
33 Q. C. Zhang, L. H. Li, H. Li, L. Tang, B. He, C. W. Li, Z. H. Pan, Z. Y. Zhou, Q. L. Li, J. Sun, L. Wei, X. Fan, T. Zhang and Y. G. Yao, *Nano Energy*, 2019, **60**, 267–274.
34 A. Levitt, D. Hegh, P. Phillips, S. Uzun, M. Anayee, J. M. Razal, Y. Gogotsi and G. Dion, *Mater. Today*, 2020, **34**, 17–29.
35 D. Tobjork and R. Osterbacka, *Adv. Mater.*, 2011, **23**, 1935–1961.
36 X. Zang, C. Shen, Y. Chu, B. Li, M. Wei, J. Zhong, M. Sanghadasa and L. Lin, *Adv. Mater.*, 2018, **30**, 1800062.
37 L. B. Hu and Y. Cui, *Energy Environ. Sci.*, 2012, **5**, 6423–6435.
38 J. P. Liu, C. Yang, H. Y. Wu, Z. Y. Lin, Z. X. Zhang, R. H. Wang, B. H. Li, F. Y. Kang, L. Shi and C. P. Wong, *Energy Environ. Sci.*, 2014, **7**, 3674–3682.
39 M. M. Hamedi, A. Ainla, F. Guder, D. C. Christodouleas, M. T. Fernandez-Abedul and G. M. Whitesides, *Adv. Mater.*, 2016, **28**, 5054–5063.
40 A. Rida, R. Vyas, L. Yang, C. Kruesi and M. M. Tentzeris, *Eur. Wirel. Technol. Conf.*, 2008, 294.
41 S. Yong, J. Y. Wang, L. J. Yang, H. Q. Wang, H. Luo, R. J. Liao and Z. L. Wang, *Adv. Energy Mater.*, 2021, **11**, 2101194.
42 Y. Wang, X. Y. Liu, Y. W. Wang, H. Wang, H. Wang, S. L. Zhang, T. C. Zhao, M. Y. Xu and Z. L. Wang, *ACS Nano*, 2021, **15**, 15700–15709.
43 Y. Zi, H. Guo, Z. Wen, M. H. Yeh, C. Hu and Z. L. Wang, *ACS Nano*, 2016, **10**, 4797–4805.
44 R. Hinchet, H. J. Yoon, H. Ryu, M. K. Kim, E. K. Choi, D. S. Kim and S. W. Kim, *Science*, 2019, **365**, 491–494.
45 J. R. Huang, X. X. Yang, J. R. Yu, J. Han, C. K. Jia, M. Ding, J. Sun, X. L. Cao, Q. J. Sun and Z. L. Wang, *Nano Energy*, 2020, **69**, 104419.
46 J. Cheng, W. Ding, Y. Zi, Y. Lu, L. Ji, F. Liu, C. Wu and Z. L. Wang, *Nat. Commun.*, 2018, **9**, 3733.
47 C. G. Zhang, L. X. He, L. L. Zhou, O. Yang, W. Yuan, X. L. Wei, Y. B. Liu, L. Lu, J. Wang and Z. L. Wang, *Joule*, 2021, **5**, 1613–1623.
48 D. Li, C. Xu, Y. Liao, W. Cai, Y. Zhu and Z. L. Wang, *Sci. Adv.*, 2021, **7**, eabj0349.
49 F. B. Xi, Y. K. Pang, W. Li, T. Jiang, L. M. Zhang, T. Guo, G. X. Liu, C. Zhang and Z. L. Wang, *Nano Energy*, 2017, **37**, 168–176.
50 Z. L. Wang, *Nano Energy*, 2020, **68**, 104272.
51 X. Fan, J. Chen, J. Yang, P. Bai, Z. L. Li and Z. L. Wang, *ACS Nano*, 2015, **9**, 4236–4243.
52 C. Chen, D. Howard, S. L. Zhang, Y. Do, S. Sun, T. Y. Cheng, Z. L. Wang, G. D. Abowd and H. Oh, Tei'20: Proceedings of the Fourteenth International Conference on Tangible, Embedded, and Embodied Interaction, 2020, DOI: **10.1145/3374920.3374946**, pp. 431–442.
53 J. Ye, H. Tan, S. Wu, K. Ni, F. Pan, J. Liu, Z. Tao, Y. Qu, H. Ji, P. Simon and Y. Zhu, *Adv. Mater.*, 2018, **30**, 1801384.
54 X. Y. Shi, S. F. Pei, F. Zhou, W. C. Ren, H. M. Cheng, Z. S. Wu and X. H. Bao, *Energy Environ. Sci.*, 2019, **12**, 1534–1541.
55 L. Migliorini, C. Piazzoni, K. Pohako-Esko, M. Di Girolamo, A. Vitaloni, F. Borghi, T. Santaniello, A. Aabloo and P. Milani, *Adv. Funct. Mater.*, 2021, **31**, 2102180.